Low Stress Abrasion-Corrosion of High-Cr White Cast Iron: Combined Effects of Particle Angularity and Chloride Ions

Mobin Salasi, [1,2,z] **Mariano Iannuzzi,** [2] **William Rickard,** [3] **and Zakaria Quadir** [3]

[1]*School of Civil and Mechanical Engineering, Curtin University, Perth, Australia*
[2]*Curtin Corrosion Centre, Curtin University, Perth, Australia*
[3]*John De Laeter Centre, Curtin University, Perth, Australia*

Tribo-electrochemical behavior of a high chromium white cast iron (high-Cr WCI) used in, e.g., slurry pumps in mining and mineral processing applications, was investigated using a combination of electrochemical techniques, including zero resistance amperometry as well as potentiostatic and potentiodynamic polarisation. The effects of third body particles angularity on the localised tribocorrosion response of the cast alloy was studied during and post abrasion-corrosion by round ceramic beads and semi-angular silica sand particles. Advanced characterization methods such as electron backscatter diffraction and focused-ion beam cross-sectioning of affected areas were also employed to understand the wear and corrosion interactive actions. It was found that in chloride-free solutions, the behavior of high-Cr WCI resembled that of the austenitic 316 SS studied before. In contrast, in chloride-containing electrolytes, the semi-angular silica sand particles increased interfacial (carbide/matrix) localised corrosion susceptibility during and post-abrasion as indicated by the stark increase in anodic current and the morphology of the attack. Semi-angular silica sand abrasives had a greater adverse impact on post-abrasion interfacial corrosion vulnerability, compared to round ceramic beads. The complex behavior observed indicates that any material developed for tribocorrosive conditions must account for the particles angularity and their subsequent effects on localised corrosion.

High chromium white cast irons (high-Cr WCI) are commonly used in applications where abrasion and corrosion concurrently occur; e.g. slurry pumps in mining and mineral processing applications.[1] The microstructure of high-Cr WCIs consists of a tough matrix and a combination of hard carbides.[2] The matrix of these alloys usually contains sufficient amounts of solute Cr, which enables formation of a nanoscale protective passive oxide film and therefore exhibiting a "stainless" behavior.[3] Although the combination of such properties (i.e., hard carbide surrounded by a tough passive matrix) would entail excellent wear-only[4–6] and corrosion-only[6,7] properties, these materials regularly fail in-service.[8] Microscopic examination of worn slurry pump surfaces revealed that when used in tribocorrosive conditions, a combination of mechanisms different to that of a wear-only or corrosion-only condition led to their failure.[9] Thus, it is essential to understand the behavior of these materials prior to application where the conjoint action of wear and corrosion is anticipated.

In slurry pumps, three-body abrasion-corrosion is a common mode of tribocorrosion where the abrasive particles are trapped between two moving surfaces.[10] During three-body abrasion, abrasive particles may disrupt the passive film associated with a material displacement/removal leading to an accelerated and enduring dissolution of the matrix.[11] The accelerated dissolution of the matrix leaves the carbides unsupported, leading to their subsequent spalling in contact with abrasive particles.[12] Occasions of localised corrosion found at the carbide/matrix peripheries could also create similar issues, i.e., the carbides remain unsupported.[13]

In most cases for a single-phase passivating material (e.g., austenitic stainless steels), tribo-electrochemical methods such as open circuit potential (OCP) measurements,[14] potentiodynamic[15] and potentiostatic polarization,[16] and zero resistant amperometry (ZRA)[17] provide information on the interaction of abrasion and corrosion.[18] For example, revealing the effects of mechanical factors such as wear mechanisms, particles motion and angularity on disruption and repair of the passive film, and detecting possible localised corrosion post abrasion-corrosion process are a few benefits of these methods.[19]

In contrast to single-phase systems, for multiphase alloys such as high-Cr WCI, a combination of experimental methods is needed to account for the several tribocorrosion mechanisms that could be potentially occurring.[9,20] Interaction of the solid particles with the high-Cr WCIs multiphase microstructure and the non-uniformly distributed

passive film on their surface is complex and difficult to understand.[21] Particles with different angularity are commonly present in the pumped slurries and their interactions with the high-Cr WCI surface in a corrosive environment are poorly understood. Moreover, these alloys are often prone to localised corrosion,[13] which can be aggravated by abrasion. For example, understanding whether worn surfaces could potentially incur in different post-abrasion localised corrosion behavior is difficult to assess experimentally and requires further research.[9]

The objective of this work was to differentiate the individual effects of localised corrosion and abrasion-corrosion occurring on the high-Cr WCI multiphase alloy. The effects of round and semi-angular coarse abrasive particles on the three-body abrasion-corrosion of these materials in a moderately alkaline solution with and without chloride ions are investigated. Electrochemical techniques including potentiostatic polarization and ZRA were employed. Scanning electron microscopy (SEM) and focused ion beam (FIB) methods were, then, used to analyze the worn surfaces and to gain a better understanding of the subsurface deformation and localised dissolution.

Experimental

Materials and solution.—Tests were carried out in 0.2 M Na_2CO_3 buffered solution with varying NaCl concentrations of 0, 10, and 36 g/l, respectively named solutions A, B, and C. The base test solutions are similar to that often found in alumina processing applications.[22] The measured pH of the solutions was 11.2 ($\pm$0.2), independent of the Cl^- content. To prepare the solutions, analytical reagent (AR) grade chemicals (Na_2CO_3 and NaCl) were mixed in ultrapure (17.4 MΩ) water.

A hypereutectic as cast high-Cr white cast iron with an initial 30% Cr and 4.5% C was used in this study. Likewise, a single-phase martensitic 13Cr stainless steel (UNS S4100) with a nominal composition of 11.5–13.5 wt% Cr, <0.15 wt%, <1.0 wt% Mn, <1.0 wt% Si, bal. Fe was used as a reference system for electrochemical testing as discussed below. The actual composition and the microstructure of both alloys were characterized in detailed using a combination of techniques.

Chemical composition of the high-Cr WCI matrix and the 13Cr SS was characterized using quantitative energy dispersive spectroscopy (EDS). The quantitative EDS was performed following cobalt calibration, on a flat polished surface using a Zeiss Neon field-emission scanning electron microscope (FE-SEM) equipped with an Oxford detector. The quantification was performed using AZtec software.
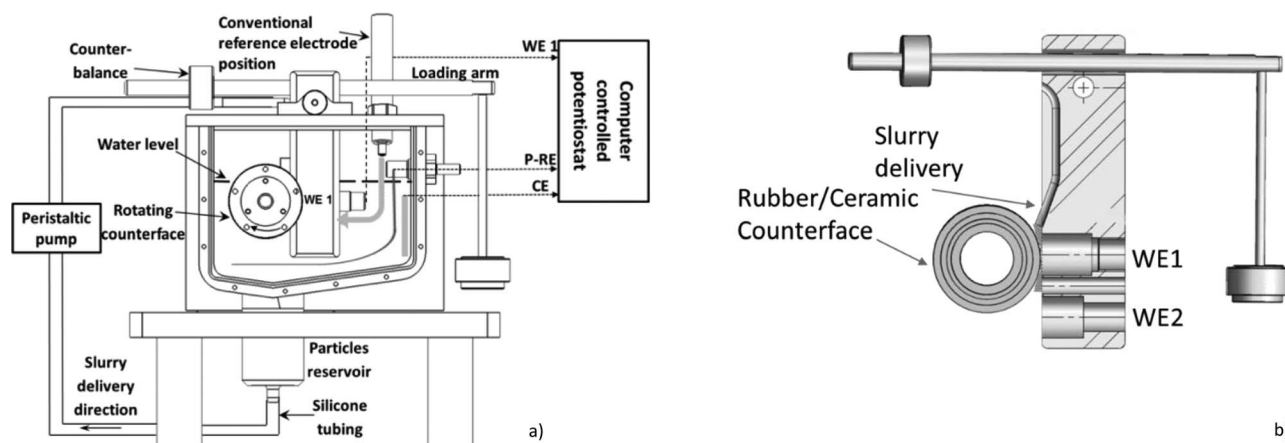
z E-mail: mobin.salasi@curtin.edu.au

Figure 1. Tribo-electrochemical test rig used for the low-stress abrasion-corrosion studies: a) the test rig, b) close up view.

The microstructure of a finely polished high-Cr WCI (up to 0.3 μm colloidal silica suspension) was imaged using a secondary electron (SE) and electron backscatter diffraction (EBSD) detector in a FE-SEM TESCAN MIRA3 equipped with an Oxford Symmetry EBSD detector.

X-ray diffraction analysis was performed using a Diffractometer D8 Advance (Bruker AXS, Germany), with a copper K alpha radiation source (at 40 kV & 40 mA) with a LynxEye detector. The scanning range was 30 to 90° with increments of 0.015 degrees and the time per step was 0.7 s.

The high-Cr WCI and 13Cr materials were wire-cut to 12 mm diameter samples and a surface area of 1.13 cm^2 was exposed to the test solution. An insulated wire was connected to one side of the samples using carbon paste and left for curing overnight. Afterwards, samples were mounted in an epoxy resin. Prior to the tests, samples were wet-ground up to 1200 grit SiC abrasive paper and subsequently rinsed with ethanol and ultrapure water.

Tribo-electrochemical test rig.—The tribo-electrochemical test rig, described elsewhere,[19] was employed to investigate three-body abrasion-corrosion of the high-Cr WCI (see Figure 1). Round ceramic beads and semi-angular silica sand coarse abrasive particles were delivered to the interface between the samples tested (WE1) and a rotating rubber counterface with tangential speed of 61 mm/s. During three-body abrasion tests, the wear scar had an approximate apparent surface area of 10 × 6 mm. To achieve the required size, silica sand abrasive particles were sieved to 212–300 μm and the round ceramic beads were purchased at a size range of 200–300 μm. The angularity of the particles was characterized using spike-quadratic (SPQ) fit method[23] and circularity factor analysis (CFA),[24] and the results are given in Table II. The SPQ method isolates the boundary features protruding outside the average-radius circle of each particle. Quadratic segments are, then, fitted to both sides of each spike and differentiated; the cosine of half the apex angle, called 'spike value' (SV), is used as a measure of the spike's angularity. The A_{SPQ} value for a particle was averaged over all individual SVs. A minimum of 20 particles SPQ were averaged. The circularity factor, on the other hand, was defined as: $\frac{4\pi A}{P^2}$; where A is the projected abrasive particle area and P is its perimeter. A_{SPQ} and CFA analyses were conducted using commercially available software packages, namely Matlab and ImageJ, respectively.

Electrochemical tests.—A SP300 Biologic bipotentiostat equipped with a low current cable was employed to conduct the corrosion-only and tribo-electrochemical tests. A double junction Ag/AgCl (sat. KCl) electrode (SSE) was used as the reference. This electrode's potential was 0.253 V against the saturated hydrogen electrode (SHE). A platinum wire was used as the counter electrode (CE) in the cyclic polarization and potentiostatic polarization experiments.

The following electrochemical parameters were utilised for corrosion-only and abrasion-corrosion investigations. Electrochemical tests were conducted in duplicate to address reproducibility.

Cyclic polarization.—Cyclic polarization was employed to evaluate the corrosion-only response (i.e., passivity and localised corrosion behavior) of the samples. The sample's potential was scanned at a rate of 1 mV/s from 0.1 V below the OCP until the current density reached 1 mA/cm^2. Then, the potential was reversed. The experiment was stopped when the potential reached the initial OCP. The mean current measured over the last 25% of the step duration, was averaged over 5 voltage steps as recommended by the equipment manufacturer.

ZRA tests.—ZRA was used to quantify the current flow between two working electrodes, namely WE1 and WE2, before, during, and after three-body abrasion-corrosion tests. The WE1 could undergo low-stress abrasion-corrosion once loaded against the rotating rubber counterface while the WE2 was freely exposed. WE1's corrosion-only behavior was studied while it was unloaded, the particles were continually fed through the interface of the WE1 and the rubber counterface was rotating at 61 mm/s. In the ZRA measurements, two dissimilar electrodes (i.e. one multiphase high-Cr WCI and one single phase 13Cr stainless steel) were used instead of the two identical electrodes previously adopted.[21] The premise is that the 13Cr SS would have a priori similar passive behavior to that of the high-Cr WCI matrix given their similar Cr content (refer to these alloys Cr content given in Table I). Additionally, it was anticipated that the single-phase 13Cr SS would have a better localised corrosion resistance than that of the high-Cr WCI. Hence, the localised corrosion events could be isolated on the WE1. This assumption was verified in this study and a detailed explanation is given in the Discussion (ZRA method used in this study section).

The two electrodes (WE1 and WE2) were periodically coupled and de-coupled during the ZRA monitoring. When coupled, fluctuations in potential and current were recorded. For the de-coupled samples, independent potential changes of the WE1 and WE2 were concurrently recorded as a function of time. The de-coupling potential measurement

Table I. Chemical composition of high-Cr WCI matrix and 13Cr stainless steel, measured by quantitative EDS.

Material	Chemical composition (in wt%; Fe bal.)
Matrix of high-Cr white cast iron	Cr: 12.2, Si: 0.9, S: 0.2, Mn: 2.3 (austenitic)
13Cr stainless steel	Cr: 12.6, Si: 0.3, Ni: 6.2, Mo: 2.1 (martensitic)

Table II. Characteristics of abrasive particles used in the three-body abrasion-corrosion experiments.

Abrasives	Size (μm)	Hardness ($HV_{0.2}$)	A_{SPQ}	CFA
Ceramic beads (CB)	200–300	1250	0.04	0.961
Silica sand (SiSa)	212–300	1220	0.25	0.709

was used to monitor the separate WE1 and WE2's potential (E_{WE1} and E_{WE2}).[25] During the tests an internal 5 Hz analogue filter was applied to avoid non-electrochemical noise interference.[26] The potential and current data were recorded at a 2 Hz sampling frequency.

Potentiostatic polarization.—Potentiostatic polarization was employed to evaluate both corrosion-only and abrasion-corrosion conditions. The time evolution of the current response of the samples was measured before, during, and after abrasion-corrosion tests while the sample's potential was held constant at −0.1 V/SSE. The data acquisition frequency was 2 Hz.

Post abrasion-corrosion characterization.—A FE-SEM was used to examine tribocorroded surfaces. To visualise the sub-surface, a Tescan Lyra3 focused ion beam (FIB) was used to expose cross-section at the regions of interest; i.e. along carbide/matrix interphase. As per the standard FIB protocol, a platinum strip was first deposited over the region of interest, then FIB was used to sputter away a trench of approximately 10–15 μm wide and 8 μm deep. Finally, 1 nA ion
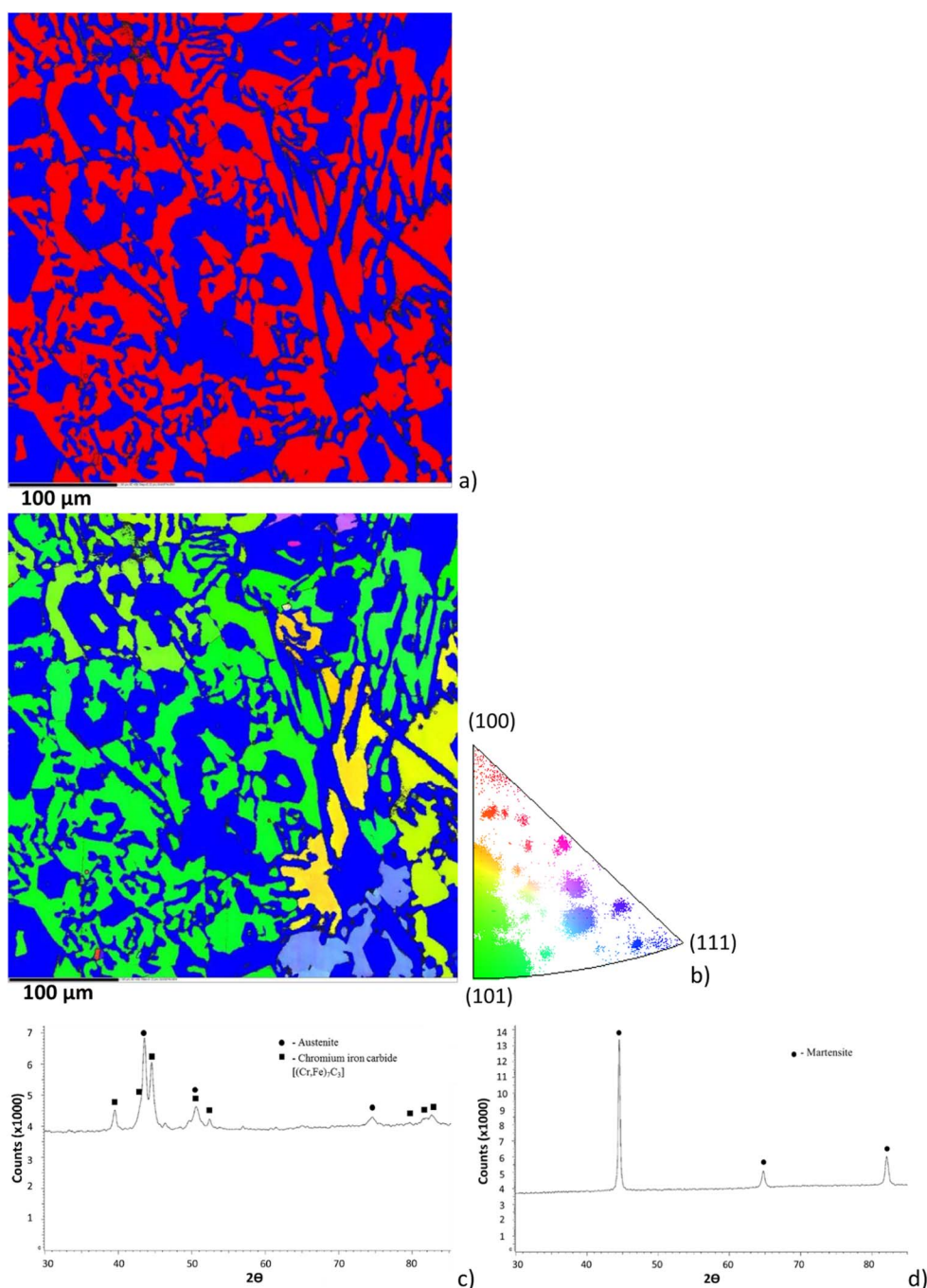

Figure 2. a and b) EBSD phase and inverse pole figure (IPF) maps of hypereutectic high-Cr WCI microstructure, c and d) X-ray diffraction patterns of the phases present in the high-Cr WCI and 13Cr SS, respectively.

Table III. Summary of parameters extracted from the cyclic polarization data results.

	E_{corr} (V/SSE)		I_{corr} (μA)		E_b (V/SSE)		E_r (V/SSE)	
	13Cr	HCWCI	13Cr	HCWCI	13Cr	HCWCI	13Cr	HCWCI
A. 0.2 M Na$_2$CO$_3$	−0.20 (±0.01)	−0.18 (±0.04)	1.86 (±0.62)	1.72 (±0.71)	0.41* (±0.04)	0.21* (±0.02)	0.09 (±0.23)	−0.12 (±0.03)
B. 0.2 M Na$_2$CO$_3$ + 10 g/L NaCl	−0.37 (±0.01)	−0.37 (±0.01)	0.98 (±0.4)	1.22 (±0.2)	0.36** (±0.02)	0.16** (±0.02)	−0.34 (±0.05)	Below E_{corr}
C. 0.2 M Na$_2$CO$_3$ + 36 g/L NaCl	−0.28 (±0.08)	−0.20 (±0.04)	2.88 (±0.74)	7.99 (±0.43)	0.02** (±0.04)	NA	−0.34 (±0.02)	NA

*Transpassive potential.
**Breakdown due to localised corrosion.

beam current was used to smooth the newly created cross-section surface. The surface was finally examined with both SE and Ion beam channelling contrast (ICC) imaging.

Results

Chemical composition.—Table I provides the elemental analysis of 13Cr stainless steel and the matrix of the high-Cr WCI used in this study, measured by quantitative EDS. It can be seen that a similar quantity of solute Cr was available (>12 wt%) within the matrix of the high-Cr WCI and the bulk of 13Cr SS; sufficient to achieve a borderline passivity in chloride containing environments on both materials.[27]

Materials and abrasive particles characterization.—Figure 2a shows an EBSD measured phase distribution map of the as-cast hypereutectic high-Cr WCI. Overall, the austenite matrix and the Cr$_7$C$_3$ carbides occupied almost at equal area fraction. As seen in Figure 2a, austenite areas (in red) were surrounded by the primary and eutectic carbides (blue areas). An inverse pole figure (IPF) orientation map of austenite is presented with a color-coded pole figure in Figure 2b. The IPF analysis showed single grains spanning over austenite networks as indicated by the same grain orientation. An orientation preference of the cast structure may also prevail, but the data was insufficient to draw a firm conclusion. In agreement with the EBSD phase mapping, the diffraction pattern of high-Cr WCI was multiphase with the prevalent austenitic matrix (Figure 2c). On the contrary, 13Cr had a martensitic crystal structure (Figure 2d).

FE-SEM images of the abrasive particles used in this study (ceramic bead (CB) and silica sand (SiSa)) are shown in Figure 3 and their characteristics are tabulated in Table II. The two abrasives had a similar micro-hardness and size but their angularity was quantified to be different.

Cyclic polarization tests.—The overlayed CP plots of high-Cr WCI and 13Cr SS samples, tested in moderately alkaline buffered solutions A-C (pH 11.2 (±0.2)) are illustrated in Figures 4a–4c. A summary
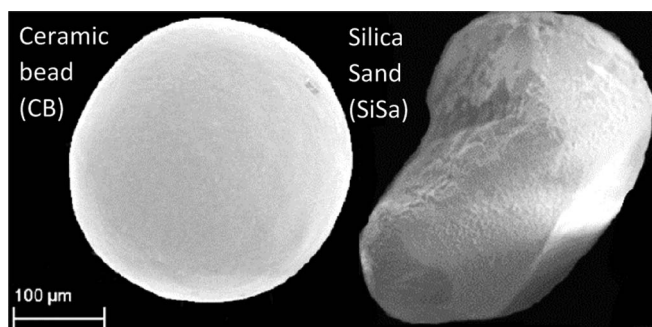

Figure 3. Secondary electron (SE) SEM images of a ceramic bead (CB) and silica sand (SiSa) particle.
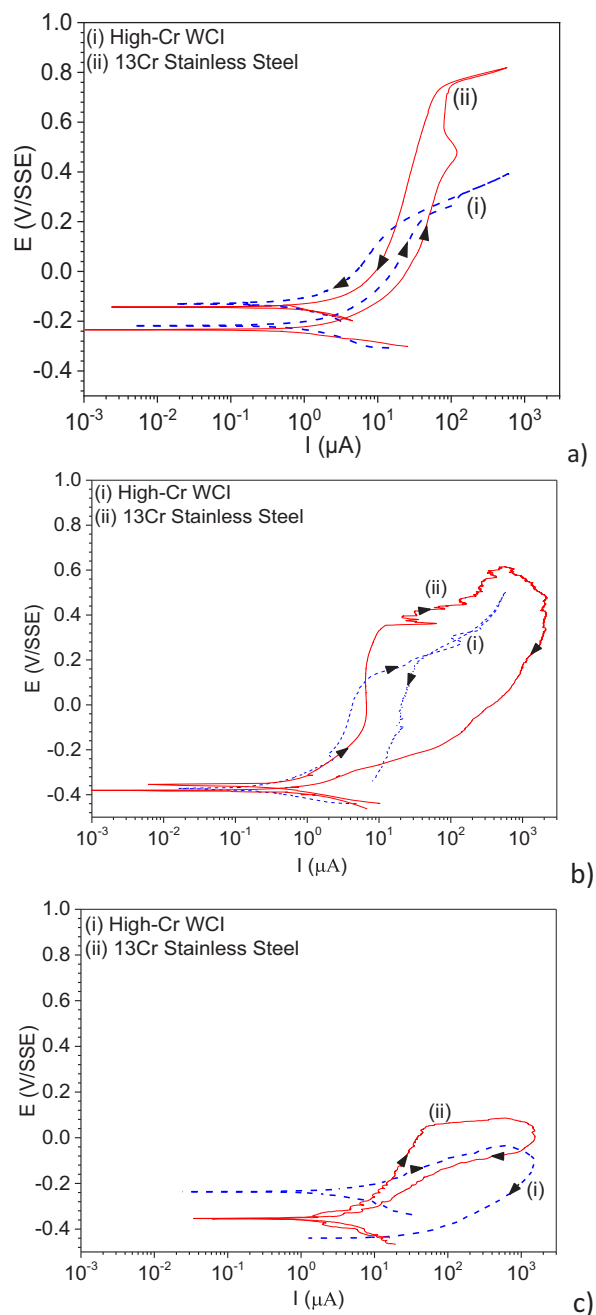

Figure 4. Cyclic polarization curves of the high-Cr WCI and 13Cr SS samples tested in 0.2 M Na$_2$CO$_3$ with a) 0, b) 10, and c) 36 g/l of NaCl; i.e. solutions A-C.
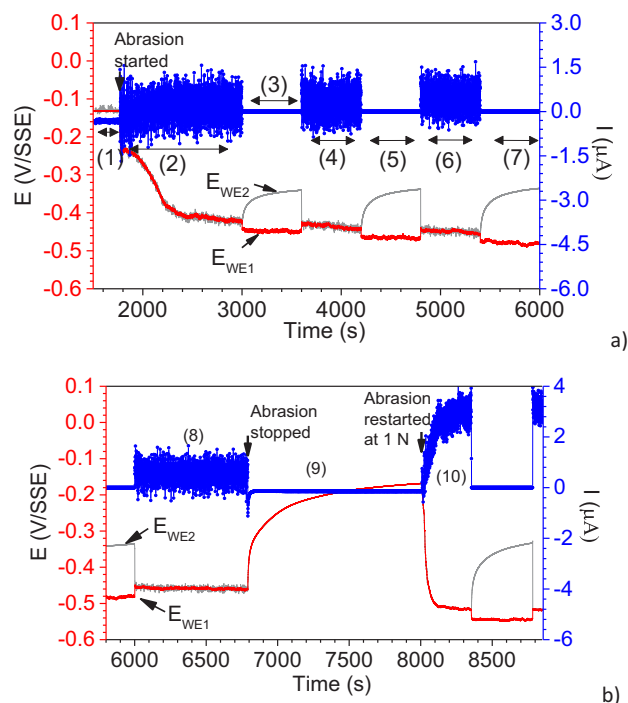
Figure 5. Galvanic current and potential changes with time measured by ZRA. Tests were carried out in solution A (0.2 M Na$_2$CO$_3$, 0 g/l NaCl). SiSa was the third body abrasive particle. E$_{WE1}$ and E$_{WE2}$ denote decoupled potential of WE1 (high-Cr WCI) and WE2 (13Cr SS) electrodes, respectively.

of parameters extracted from the CP curves; i.e., corrosion current, I$_{corr}$, corrosion potential, E$_{corr}$, breakdown potential, E$_b$, and repassivation potential, E$_r$, calculated according to the methods described previously,[28,29] are given in Table III.

As shown in Figure 4a and Table III, in solution A, I$_{corr}$, and the E$_{corr}$ values of the two materials were almost identical (around 2.4 μA and −0.2 V/SSE, respectively). The current measured within the passive region, I$_p$, was also comparable, indicating that both materials exhibited a similar passivation behavior. Neither of the two CP curves indicated localised corrosion vulnerability; i.e. the E$_b$ represents transpassive dissolution where conversion of CrIII to CrVI and oxygen evolution took place.[27,30] Two different E$_b$ (i.e., transpassive potential) values were visible, such that the single-phase 13Cr had a wider passive region than the multiphase high-Cr WCI. Both materials showed a secondary passivation following the transpassive dissolution, though it occurred at different potential ranges of approximately 0.41 and 0.28 V/SSE for the 13Cr and high-Cr WCI, respectively.

In solution B (10 g/L NaCl), both materials had a similar E$_{corr}$ ≈ −0.38 V/SSE, lower than that found in the chloride-free solution A. In the presence of chloride ions and for both materials, E$_b$, indicates localised corrosion. The high-Cr WCI showed a lower E$_b$ and E$_r$ compared to 13Cr. Both materials had similar I$_p$ in the 5–6 μA range.

As seen in Figure 4c and Table III, the I$_{corr}$ of high-Cr WCI in the solution C was around 2.5 times higher than the 13Cr SS, even though it was still within a typical passivity current range of stainless steels (≈8 μA). In solution C, the E$_{corr}$ of the high-Cr WCI was within the passive region but the material did not indicate a distinct passive region and E$_r$ was as low as −0.44 V/SSE. The higher E$_{corr}$ of high-Cr WCI, possibly suggested that the material was within the passive region, but it would not repassivate following the film breakdown.[28]

For the 13Cr SS the CP curve showed a narrow passive region and the material repassivated at E$_{corr}$ during the reverse scan.

***Tribocorrosion tests without chlorides (solution A).—**ZRA tests.*—The current and potential time evolution of tests conducted in solution A (0.2 M Na$_2$CO$_3$) are presented in Figure 5. The CP re-

sults presented above suggested that, in this solution, both materials (high-Cr WCI and 13Cr SS) were not susceptible to localised corrosion (Figure 4a). Different stages of the tests are denoted in Figure 5. In stage 1, the two electrodes were coupled under corrosion-only conditions; i.e. an unloaded WE1 was coupled to the WE2. SiSa particles were continuously fed through the interface of the sample (WE1) and the rotating counterface even though WE1 was unloaded. At this stage, only a small galvanic current was measured, since both samples have a similar passivating behavior as shown in Figure 4a.

Applying a 0.5 N load at stage 2 resulted in a current increase and high amplitude current oscillations. A peak-to-peak current value of 2.3 μA was measured at stage 2 compared to 0.09 μA in stage 1. The mean current increased to 0.4 μA, from a negative coupling current measured in the pre-abrasion-corrosion (stage 1). After a short running-in period, the potential of the coupled electrodes stabilised at values cathodic to the E$_{corr}$ of the samples (see Figure 4a). In stage 3, the two electrodes were de-coupled (i.e. the current measured was zero) while the potential fluctuations of WE1 (E$_{WE1}$) and WE2 (E$_{WE2}$) were independently recorded. Under abrasion, the de-coupled E$_{WE1}$ shifted further in the negative direction while the potential of E$_{WE2}$ (i.e., 13Cr) returned to positive potential values; albeit lower than the pre-abrasion potential. The coupling and de-coupling sequence continued for three more cycles in stages 4 to 8 where a similar pattern of behavior was observed (see Figures 5a and 5b).

In stage 9 (Figure 5b) abrasion stopped while the two electrodes remained coupled. The coupled potential immediately shifted in the positive direction; reaching values close to the pre-abrasion potential, i.e. approximately −0.16 V/SSE. At the same time, a sudden negative current shift, which almost immediately recovered, was seen just after abrasion stopped, perhaps due to a sudden capacitive discharge[31] of the passive WE2 (13Cr).

Abrasion recommenced in stage 10 (Figure 5b) at a higher applied load of 1 N. At this load and after a short running-in period of approximately 200 s, a significant increase in the evolved current occurred, reaching a mean current of approximately 3.2 μA. This value is 8 times greater than that measured at 0.5 N applied load.

***Potentiostatic tests with different angularity particles.*—**The potentiostatic current with time perturbation measured before, during, and after abrasion-corrosion of high-Cr WCI by round CB particles is shown in Figures 6a and 6b. At the pre-abrasion stage, the net passive current measured was approximately 0.92 μA. Immediately after abrasion commenced, the coupled current shifted in the anodic direction with a peak current of 8.42 μA. The mean current decreased and reached steady state at around 1.86 μA; just a slight current increase to that of the passive current before abrasion. During abrasion, the current oscillated in both positive and negative directions. When the applied load was increased to 5 N, see Figure 6b, the peak current measured increased to 29.84 μA; more than 3 times that of the 0.5 N. At this load after 400 s of abrasion-corrosion the mean current reached a steady value of 12.32 μA. The 5 N load was selected to achieve a dominating grooving wear mechanism as was observed before for AISI 316L (UNS S31603) stainless steel under the same tribo-contact.[11]

The time evolution of abrasion-corrosion current of high-Cr WCI before, during and after loading the SiSa particles are shown in Figures 6c and 6d. In contrast to the tests with CBs, no peak current was observed following sample loading; however, the total current did increase. Figures 6c and 6d also indicated that increasing the applied load from 0.5 to 5 N led to approximately 20 times increase in the mean current, i.e, from 10 μA and 220 μA when applying a 0.5 or 5N load, respectively.

Comparing Figures 6a and 6b with Figures 6c and 6d reveals that the effects of increased load on the current response was far more pronounced with the SiSa particles than the round CBs. Additionally, current oscillated around a mean value in both anodic and cathodic directions in the presence of SiSa, while for the CB particles the current oscillations were mainly in the anodic direction.
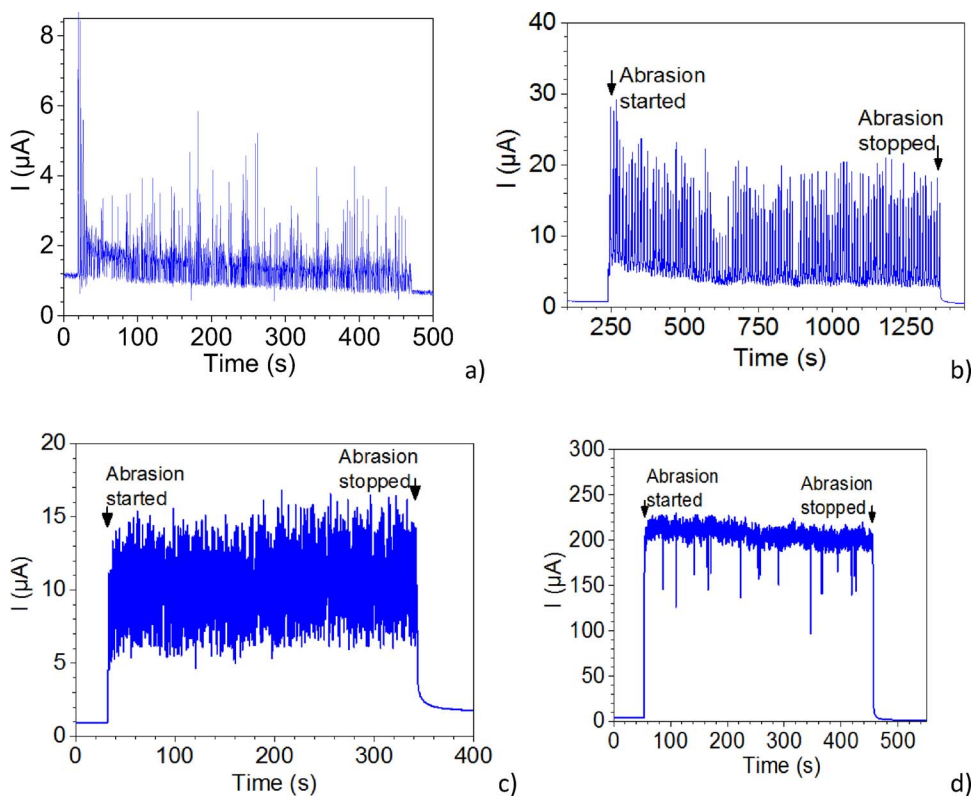
Figure 6. Three body abrasion-corrosion tests of high-Cr WCI sample at applied loads of a) 0.5 and b) 5 N with CBs and c) 0.5 and d) 5 N with SiSa against the rotating rubber counterface having a 61 mm/s tangential speed. Tests were done at −0.1 mV/SSE.

FE-SEM images of high-Cr WCI abraded at an applied 0.5 N load by CBs and SiSa particles are shown in Figure 7. As expected, there were no signs of localised dissolution within the wear scar on either test. Material removal with CBs was insignificant; supported by the observation that the grinding marks were still present (Figure 7a). In the case of SiSa particles, a smoothened matrix, and some grooves can be seen. The protruded carbides (composition verified by EDS, but not shown in the Figure) suggested that material removal was mainly concentrated on the matrix.

Tribocorrosion tests with chlorides (Solution C).—Current and potential changes were measured under corrosion-only and abrasion-corrosion by round CB and semi-angular SiSa particles. The measurements were carried out in solution C (0.2 M Na_2CO_3 with 36 g/l of NaCl). In this solution, the CP curves (Figure 4c) indicated that even at the free corrosion potential, the high-Cr WCI (WE1) would be vul-

Figure 7. SE SEM images of the high-Cr WCI working electrode after three-body abrasion-corrosion when: a) CBs, b) semi-angular SiSa particles were delivered to the interface between the sample and the rubber counterface. Tests were carried out at 0.5 N applied load, 61 mm/s tangential speed and −0.1 V/SSE constant potential.

nerable to localised corrosion, whereas the 13Cr SS (WE2) retained a stable passive film.

ZRA tests with semi-angular SiSa abrasives.—Different stages of corrosion and three-body abrasion-corrosion are presented in Figure 8. During stages 1, 5, and 7, the two electrodes were coupled under the corrosion-only condition (an unloaded WE1 with SiSa particles recirculating). Three-body abrasion-corrosion tests were conducted when the two electrodes were coupled in stages 2, 4, and 6, and decoupled in stage 3.

Applying a 0.5 N load in stage 2, resulted in an abrupt current increase concurrent with a decrease in the galvanic current (see Figure 8a). Although abrasion-corrosion trends in solution C were comparable to those of solution A (no chlorides), the magnitude of the current was much higher in the presence of chlorides, i.e. 3.84 μA vs. 0.42 μA. In stage 6, current evolved under abrasion-corrosion reached a steady value around 3.17 μA.

Positive current spikes and potential transients in the negative direction can be seen in Figure 8b; which presents a higher magnification of stage 1. The observation can be ascribed to metastable localised corrosion events.[32,33] Because the current transients were only positive the fluctuations indicated an electron flow from WE1 (high-Cr WCI) to WE2; i.e. the WE2 (13Cr SS) acted as a preferential cathode, in agreement with the CP result.

Immediately after unloading the WE1 in stage 5, current increased in the negative direction due to repassivation of the material, see arrow (i) in Figure 8c. Subsequently, as pointed by arrow (ii), a gradual rise in current appeared; suggesting continuing localised dissolution.[34] Arrows (iii) and (iv) indicate an abrupt current rise due to an onset of passive film breakdown, followed by a secondary repassivation (current drop). This process occurred repeatedly, with a moderately increasing current slope. As seen in Figure 8c, the current reached a steady state value at approximately 8000 s, fluctuating around zero thereafter.
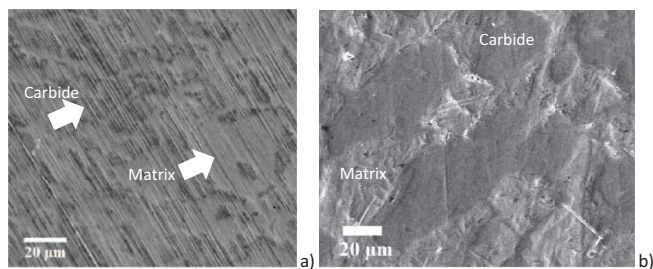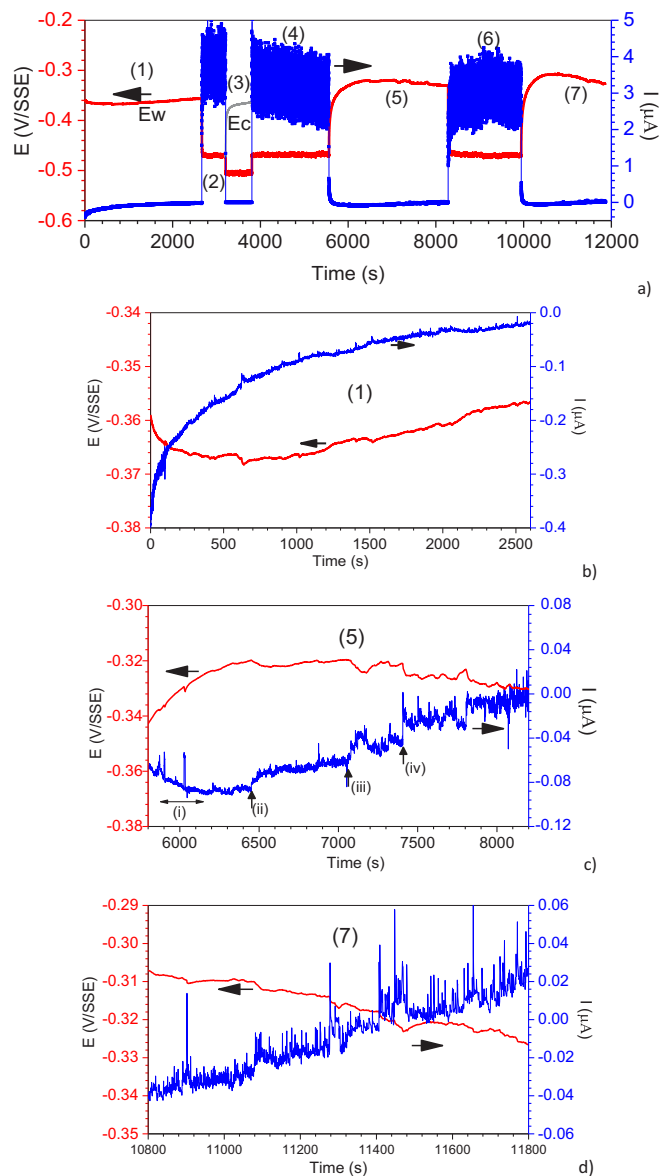
a)

b)

c)

d)

Figure 8. a) ZRA measurement before, during and after three-body abrasion-corrosion of the high-Cr WCI by semi-angular SiSa abrasive particles in solution C (0.2 M Na$_2$CO$_3$, 36 g/l NaCl). Tests were carried out under a 0.5 N applied load and rubber counterface 61 mm/s tangential speed.

In stage 7 (Figure 8d), a monotonic current rise can be seen, implying stable localised corrosion post-abrasion. Instances of current decay due to repassivation of the passive film were visible in Figure 8d.

The validity of the electrochemical data was indirectly confirmed by SEM analysis, Figure 9. A preferential mechanical removal of the matrix and areas of localised corrosion are seen. No grinding marks were found on the carbides, due to a mild polishing wear by tightly loaded SiSa abrasive particles.

Potentiostatic tests with semi-angular SiSa abrasives.—Before commencing abrasion-corrosion as shown in Figure 10, the WE (high-Cr WCI) was passivated by applying a constant potential of −0.1 V/SSE in 0.2 M Na$_2$CO$_3$ solution with 36 g/l NaCl. An applied 0.5 N load led to an abrupt current increase and high amplitude current fluctuations. The mean current reached a steady state after 1800 s, which was much shorter than the ZRA tests. Once abrasion stopped,

Figure 9. SE SEM images of the WE1 surface, following the test carried out according to the conditions in Figure 12.

an instant drop in current occurred, suggesting the repassivation of the material. However, the current gradually increased subsequently, suggesting the possibility of propagating localised corrosion, similar to what was observed in the ZRA tests. Figure 10 shows that the current slope increase in potentiostatic tests was much higher than that of ZRA exposures; i.e. 7.40 × 10^{-3} and 6.74 × 10^{-5} and µA/s in potentiostatic and ZRA tests, respectively. A plausible explanation is that during potentiostatic measurements, the potentiostat would compensate any disturbance of the potential arising from a chemical or mechanical breakdown of the passive film, by driving current through the WE. In the ZRA exposures, however, any damage to the passive film would cause an instant cathodic potential drop of the rest of the surface. The current evolved is, then, driven by spontaneous changes (reduction) in the galvanic potential between the WE1 and WE2 and the kinetics of the dissolution at the tribocorroded area on the WE1. Hence, in the ZRA measurements the magnitude of current evolved would be lower than a potentiostatic measurement under same test conditions.

The SEM image of the worn sample, Figure 11, shows areas of localised corrosion within the wear scar, supporting the potentiostatic test results.

ZRA tests with round CBs in solution C.—The current and potential time evolution of the tests conducted with round CBs are shown in Figure 12. As the two electrodes were coupled without abrasion, incidents of positive current transients with concurrent negative shifts of potential were evident in stage 1 (corrosion-only). The transients were only in the positive direction and terminated after a short period of time, (between 0.2 to 4 s). As explained above when discussing semi-angular SiSa abrasives test results (Figure 8), such transients resembled a pattern usually found during metastable localised dissolution.[35]

Introducing abrasion in stages 2 to 4 resulted in a sharp current rise and a simultaneous negative shift of potential indicating that the round
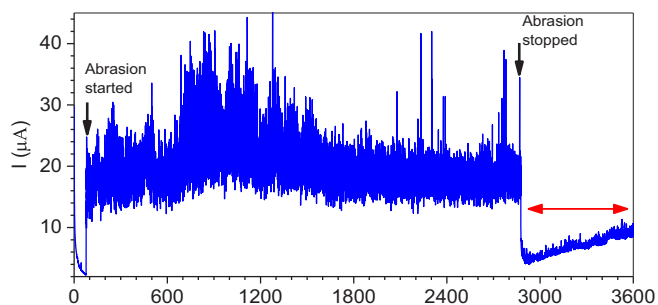

Figure 10. Time current evolution during potentiostatic polarization of high-Cr WCI tested in solution C at −0.1 V/SSE. Three-body abrasion-corrosion was carried out with SiSa abrasive particles, 0.5 N applied load and 61 mm/s counterface tangential speed.
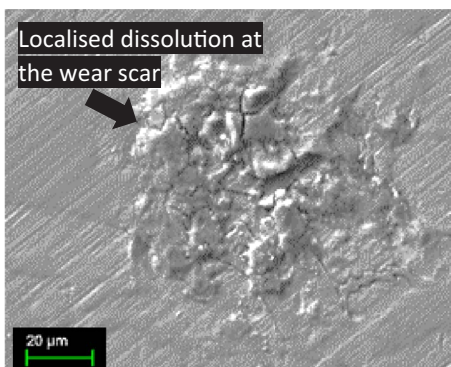
Figure 11. SE SEM images of the WE1 surface, following the test carried out in Figure 10.

CBs de-passivated the surface. This behavior is similar to the trends seen in Figure 4 in solution A (no chlorides). The de-coupling potentials of WE1 and WE2 measured in stage 3 were also in agreement with those of Figure 4a conducted in the solution A.

On the other hand, a feature specific to Figure 12 was the mean current and potential trends in stages 2–4 as the WE1 underwent abrasion. In that timeframe, the coupled potential increased (anodic shift) and the galvanic current declined in magnitude. The downward current trend measured under abrasion indicates that abrasion by hard round CBs, slowed down the dissolution kinetics instead of the anticipated accelerating action. Likewise, the separate E_{W1} and E_{WE2} shown in stage 3 exhibited a trend, again specific to abrasion-corrosion by round CBs. Thus, although the potential initially dropped it continued to increase in the positive direction with time.

Similar to the behavior observed in solution A, the current instantly dropped and the material repassivated after unloading the WE1 (stage 5-corrosion only). The current, however, gradually increased with time
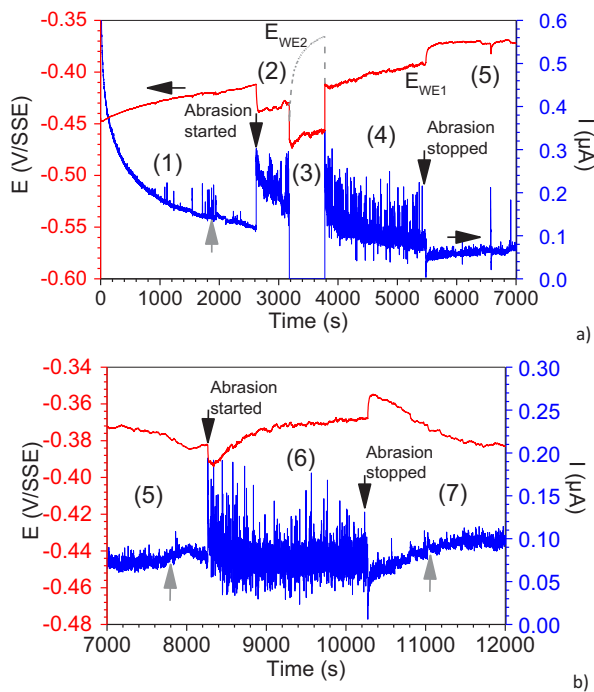
when the high-Cr WCI electrode was not under abrasion. It is also evident from Figure 12a that the current increase was associated with a negative potential shift. Several short-lived current transients are visible at this stage, similar to stage 1. An example current transient relevant to stage 5 is shown in Figure 12b. The pattern of the current transient resembles breakdown of the film, followed by repassivation.

In stage 6, the current measured during abrasion-corrosion by CBs indicates a steady response. The average current measured during abrasion was in the 0.09 μA range, associated with high amplitude current oscillations (Figure 12b). An initial current drop was detected upon unloading WE1 in stage 7, followed by a gradual current increase.

Sub-surface modification of the high-Cr WCI due to abrasion-corrosion was evaluated by site-specific cross-sectioning the samples with FIB-SEM. The cross-sectional analyses were done in different worn areas showing varying degrees of damage. The FIB-milling focus was on the boundaries between matrix and the carbide.

An area within the wear scar generated during the exposure detailed in Figure 12 was selected where there were no signs of localised corrosion, and an intact boundary were seen at the carbide/matrix interface (Figure 13a). The ICC image shown in Figure 13b revealed an approximately 200 nm deep finely-grained tribolayer and signs of subsurface deformation of the matrix.

The SE image in Figure 14a illustrates another area within the wear scar following the tests detailed in Figure 8 with two FIB-milled craters (i) and (ii). Similar to Figure 13, there were no signs of mechanical material removal or cutting wear mechanisms. Higher magnification ICC image of the crater (i) shown in Figure 14b revealed boundary dissolution of the matrix at the carbide/matrix interface. A bi-layer microstructure was found between the two carbides where the bottom layer is the residual corrosion products and the top layer indicates the matrix smeared by round ceramic beads.

The FIB-cross-section (ii) in Figure 14c shows dissolution and delamination of the matrix at the carbide peripheries, undercutting the carbides. Formation of finely-grained regions over the matrix were also seen.

The FIB-cross-section at another area shown in Figure 15a illustrates an elongated subsurface crack in the carbide and dissolution at carbide/matrix boundary. Higher magnification ICC image (Figure 15b) showed a finely-grained tribolayer formed on the surface. The SE image in Figure 15c suggested dissolution of the matrix at the carbide peripheries; the narrow crevice-like area became wider below the surface. The finely-grained tribolayer formed on the matrix had similar characteristics to those found underneath the tribo-corroded AISI 316L stainless steel after three-body abrasion-corrosion with glass beads particles.[11]

Discussion

A summary of the observations in the results obtained during the ZRA tests is given in Table IV. The implications of the findings are discussed below.

Figure 12. ZRA measurements at different stages before, during and after three-body abrasion-corrosion of high-Cr WCI (WE1) by round CBs in solution C (0.2 M Na_2CO_3, 36 g/l NaCl). Tests were carried out under a 0.5 N applied load against a rubber counterface at 61 mm/s tangential speed. Current and potential changes measured at: a) stages 1–5 b) stages 5–7.

Effects of particle angularity without chlorides.—A comparison of the results obtained in this study during potentiostatic three-body abrasion-corrosion testing of high-Cr WCI with that of a single-phase austenitic 316L SS previously reported[11] are given in Figure 16. For both materials, increasing the applied load led to a higher current response. A higher load resulted in a much more effective particle grip by the rubber counterface; hence an enhanced depassivation of the WE1 (high-Cr WCI). Previous two[36] and three-body[11] tribocorrosion studies showed that current measured was proportional to the applied load. In this investigation only two data points were obtained, insufficient to verify whether a similar correlation exists, but this was not the scope of this research.

The magnitude of current measured for high-Cr WCI was, however, lower than that of 316L SS. A possible reason is that in tribocorrosion of the high-Cr WCI depassivation only occurs on the matrix. The
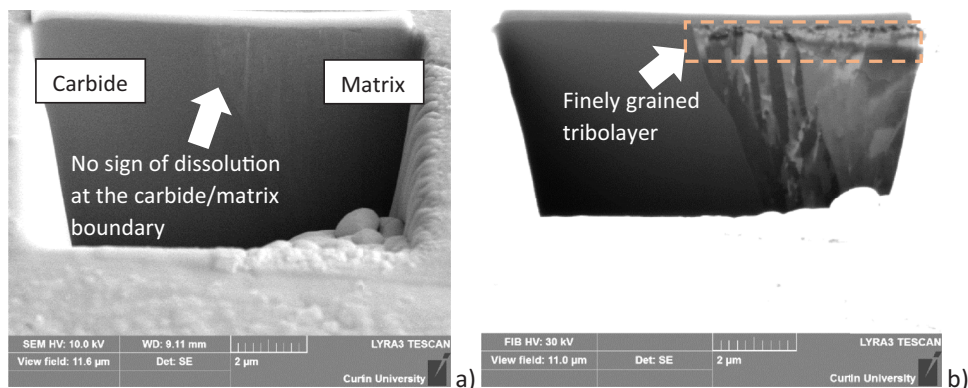
Figure 13. FIB-milled crater with the worn surface after ZRA test shown in Figure 12; a) SE SEM and b) ICC images, respectively.

hard $M(Cr,Fe)_7C_3$ carbides do not develop a uniform passive film[13] and, hence, their abrasion would have minimal contribution on current discharge. Nevertheless SEM images showed they were unaffected by abrasion. The behavior of carbides would explain the lower depassivation current discharge of high-Cr WCI in comparison to the 316L SS.

Another observation in solution A was that as soon as abrasion-corrosion stopped, the material rapidly repassivated, similar trend to a 316L SS.

ZRA method used in this study.—Conventionally, electrochemical noise studies using ZRA involve galvanically coupling two nominally identical electrodes (Figure 17a).[26] This arrangement, shown in Figure 17a, has been extensively used to monitor localised corrosion incidents; i.e. nucleation, termination or stable growth of the pits and to determine critical pitting temperature.[37,38] The polarity of the transients indicate whether localised dissolution is occurring on the WE1 or WE2; e.g. as per the most common polarity convention[39] a negative current transient indicates dissolution activity on the WE2.
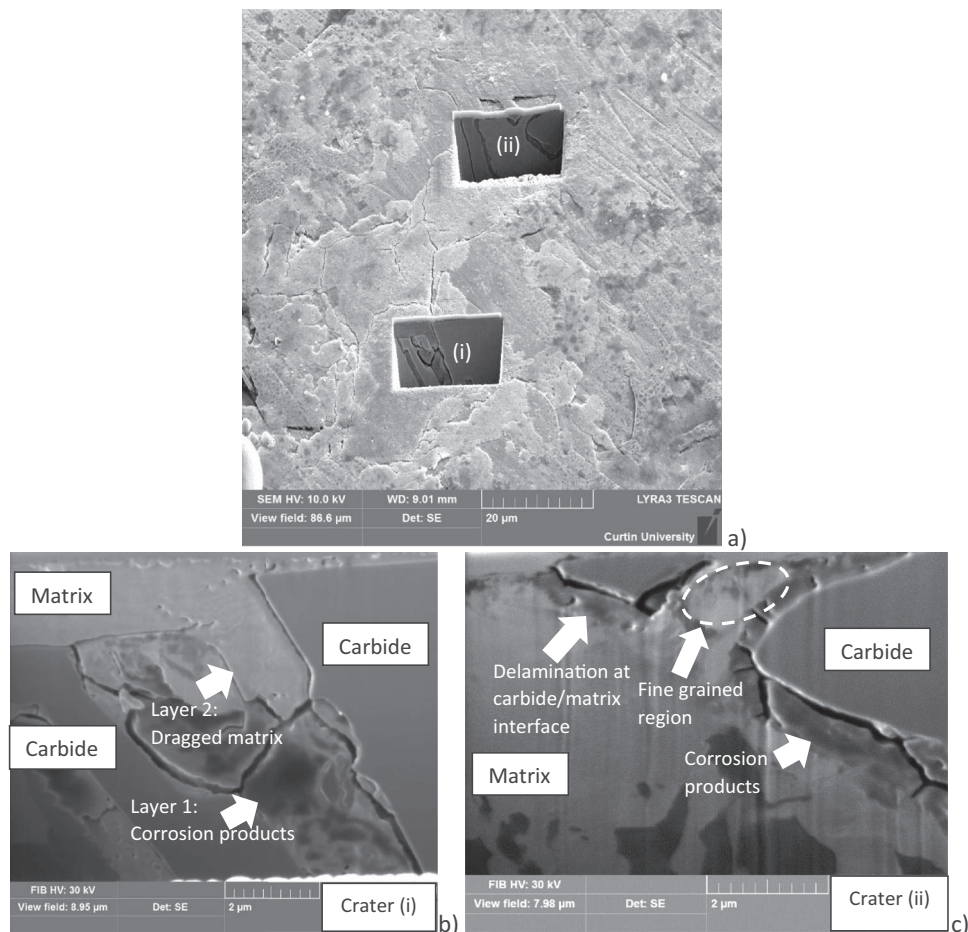

Figure 14. a) FIB-milled craters (i) and (ii) in the worn surface after ZRA tests by round ceramic beads shown in Figure 12, b) and c) higher magnification ICC images of (i) and (ii) craters, respectively.
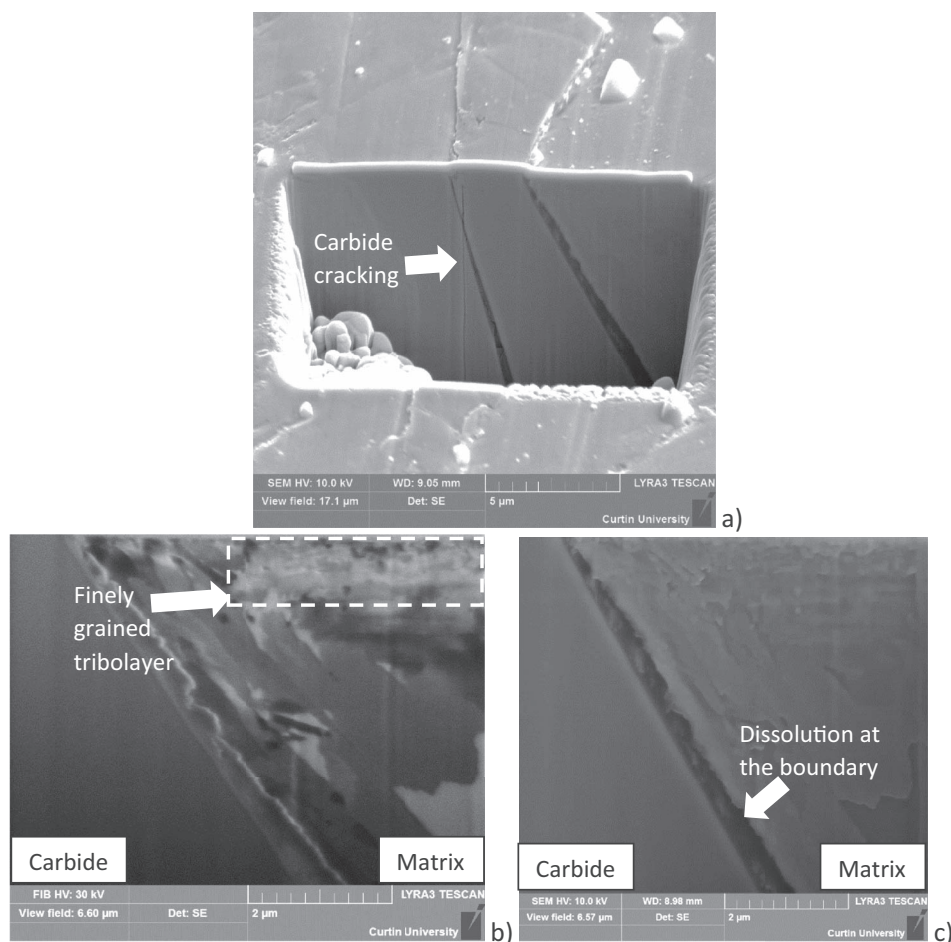
Figure 15. FIB-milled crater in the worn surface after ZRA tests by round CBs shown in Figure 12, a) crater location, b) ISE, c) SE high magnification image of the cross section.

In a tribocorrosion experiment, the WE1 undergoes abrasion-corrosion whereas the identical secondary electrode WE2 is subjected to corrosion-only, see Figure 17b.[19,40,41] Using a ZRA on such an arrangement, information can be obtained on the effects of wear on passive film removal and reformation mechanisms.[17,19,42] For example, under abrasion, an increase in the current measured indicates disruption of the passive oxide film.[43] Post abrasion, film repair is generally associated with a rapid current decay similar to those of scratch tests.[44]
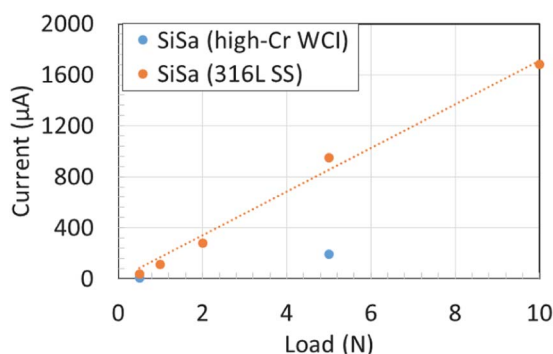

Figure 16. a) Comparison of the mean currents obtained in potentiostatic three-body abrasion-corrosion tests of high-Cr WCI and 316L stainless steel abraded by semi-angular silica sand particles. The 316L SS sample tests were carried at 61 mm/s tangential speed and −0.1 V/SSE applied potential in 3.5 wt% NaCl near neutral solution.[11]

Table IV. Summary of the ZRA tests observations for the tests carried out in solution C (0.2 M Na_2CO_3 and 36 g/l NaCl).

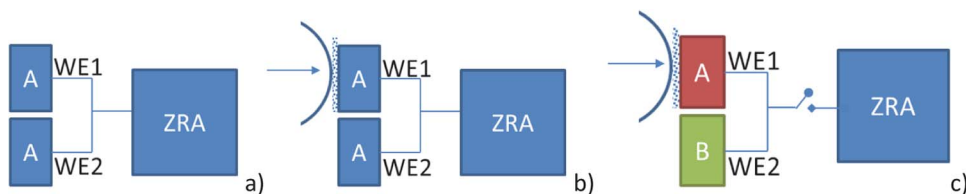|	Ceramics beads	Silica sand
Before abrasion	Short lived current transients were visible, average current was small, in the ±0.1 μA range.	
Starting abrasion	• An immediate current rise together with a concurrent cathodic shift of potential. The peak current measured was in 0.3 μA range.	• An immediate current rise together with a concurrent cathodic shift of potential. The peak current measured was in 4.8 μA range.
During abrasion-corrosion	• In the beginning, a negative current-time slope. • At steady state, the magnitude of current under abrasion was in the 0.1 μA range.	• Current reached steady state under abrasion-corrosion at a much higher magnitude, i.e., about 3.2 μA, than the corrosion-only current measured.
Post abrasion	• An instantaneous current drop for a short period of time followed by regular incidents of film breakdown and repair. Eventually with extended time a monotonic current increase was observed.	• An immediate current decay occurred, followed by a monotonic current increase.

Figure 17. a) Conventional ZRA measurement in a corrosion-only condition, the two electrodes are identical, b) abrasion-corrosion ZRA test with two identical electrode materials, c) modified ZRA measurement, dissimilar electrode materials with similar passivity were used; in b and c) WE1 undergoes abrasion while WE2 is subjected to corrosion-only.

A frequent problem with the setup shown in Figure 17b is the occurrence of current polarity reversals when both WE1 and WE2 undergo localised corrosion. Polarity reversal makes the interpretation of the results difficult.[9] Since it is known that localised corrosion susceptibility of the high-Cr WCI is due to a weakened passivity at the carbide/matrix interface[13] using a single-phase alloy as WE2 would alleviate its localised corrosion vulnerability, and is therefore, polarity reversal problems. Thus, the electrode arrangement schematically shown in Figure 17c was used in this study as explained in the Experimental section.

Combined effects of chlorides and particle angularity.—Previous studies suggested that exposure of high-Cr WCIs to solutions with different pH led to a varying corrosion resistance of the phases within their microstructure.[3,12,45–47] A summary of these observations is illustrated in Figure 18a.

In the moderately alkaline conditions tested in this research, a borderline passivity is anticipated over the matrix and the carbide/matrix boundary. Adding chlorides, on the other hand, often leads to a complex corrosion and tribocorrosion behavior of high-Cr WCIs.[21] The carbide/matrix interface has been found to have a weakened passivity, and hence, were prone to passivity breakdown in the presence of chloride ions.[13] As shown in Figure 18b, breakdown of the passive film often occurs at the carbide/matrix boundary, followed by a continued dissolution.

Combined SEM and FIB analysis indicated that the round CBs only plastically deformed the matrix rather than producing ploughing or cutting, which could subsequently lead to material removal. Although the ductile matrix was smeared on the surface by the round CBs, the damage was insufficient to attain a steady depassivation. Even as abrasion continued, a lower anodic current was measured than that recorded at the start of the abrasion. From FIB ICC imaging (Figures 13–15), it can be seen that a compacted tribolayer formed on the surface. Further research is needed to understand the nature of this layer as well as its tribocorrosion implications. The current increased gradually post-abrasion, possibly due to stable localised corrosion. The monotonic current rise stopped during abrasion cycles. It is speculated that abrasion hindered localised corrosion growth by filling the micro-crevices formed around the carbide peripheries (see FIB images shown in Figure 14). It should be noted that although the current response resembled a behavior indicative of localised dissolution

events;[48] however, the attack did not show a typical hemispherical or tri-dimensional pitting corrosion morphology as it was concentrated at the carbide/matrix interface (see Figures 13 and 14).

In the case of semi-angular SiSa particles, repeated ploughing followed by microfracture was the dominant wear mechanism. Unlike the CB tests, during abrasion-corrosion by SiSa abrasives, no declining current trend nor an upward shift of potential can be seen. Also, the semi-angular SiSa particles led to a much greater current increase than the CBs. The current measured was predominantly controlled by abrasion and the mechanical factors such as load. Post abrasion localised dissolution was found within the irregularities of the worn regions.

Interestingly the overall slope of current increase following abrasion with SiSa abrasives was higher than those of CBs. Comparing Figures 8 and 12 it can be seen that in stage 5 of SiSa, (Figure 8) there were a continuous current increase with time at a rate of 4.71×10^{-5} µA/s while that of CBs (Figure 12) showed mostly incidents of metastable film breakdown followed by repassivation. It is possible that a much rougher surface generated by hard SiSa abrasives had given rise to a more stably growing localised corrosion.

Conclusions

In this study, the combined effects of particle angularity and chloride ions on abrasion-corrosion and post-abrasion interfacial localised corrosion behavior of high-Cr WCI were investigated. Based on the findings presented above the following conclusions were drawn:

• In the absence of chloride ions, abrasion-corrosion of high-Cr WCI by both CB and semi-angular SiSa particles resembled the well-documented behavior of the single-phase austenitic 316L SS.

• In the presence of chloride ions, once abrasion-corrosion reached steady state, SiSa particles increased the net anodic current, i.e., from 3.84 µA vs. 0.42 µA, compared to that of the chloride-free solution.

• The ZRA abrasion-corrosion study of the multiphase high-Cr WCI showed that the angularity of particles might alter the post-abrasion interfacial corrosion vulnerability of the material. Semi-angular silica sand abrasives had a much greater adverse impact on the post-abrasion interfacial corrosion susceptibility than those of round ceramic beads. Any material developed for tribocorrosive conditions
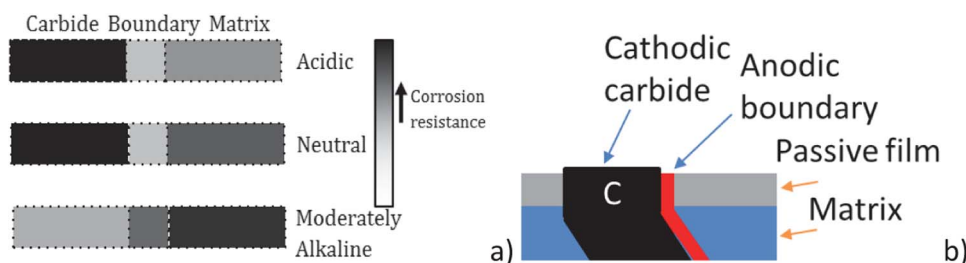

Figure 18. a) Electrochemical nobility of high-Cr WCI at different pH conditions, b) anodic and cathodic regions on the WE1 surface when tested in solution C.

should account for the angularity of particles and their subsequent effects on localised corrosion behavior.

ORCID

Mobin Salasi https://orcid.org/0000-0002-1412-4608
Mariano Iannuzzi https://orcid.org/0000-0001-9202-3696

References

1. H. H. Tian, G. R. Addie, and R. J. Visintainer, *Wear*, **267**, 2039 (2009).
2. W. H. Kan et al., *Wear*, **398–399**, 220 (2018).
3. A. Neville, F. Reza, S. Chiovelli, and T. Revega, *Metall. Mater. Trans. A*, **37**, 2339 (2006).
4. T. A. Adler and Ö. N. Doğan, *Wear*, **225–229**, 174 (1999).
5. R. J. Llewellyn, S. K. Yick, and K. F. Dolman, *Wear*, **256**, 592 (2004).
6. B. Lu, J. Luo, and S. Chiovelli, *Metall. Mater. Trans. A*, **37**, 3029 (2006).
7. E. Zumelzu, I. Goyos, C. Cabezas, O. Opitz, and A. Parada, *J. Mater. Process. Technol.*, **128**, 250 (2002).
8. G. B. Stachowiak, G. W. Stachowiak, and O. Celliers, *Tribol. Int.*, **38**, 1076 (2005).
9. G. Stachowiak, M. Salasi, and G. Stachowiak, *J. Bio- Tribo-Corrosion*, **1**, 6 (2015).
10. M. Salasi, G. B. Stachowiak, and G. W. Stachowiak, *Tribol. Lett.*, **40**, 71 (2010).
11. G. W. G. B. G. B. G. W. Stachowiak, M. Salasi, W. D. A. W. D. A. Rickard, and G. W. G. B. G. B. G. W. Stachowiak, *Corros. Sci.*, **111**, 690 (2016).
12. M. Salasi, G. B. Stachowiak, and G. W. Stachowiak, *Wear*, **271**, 1385 (2011).
13. M. Salasi, G. B. Stachowiak, G. W. Stachowiak, and M. R. Kilburn, *Corros. Sci.*, **67**, 298 (2013).
14. P. Ponthiaux, F. Wenger, D. Drees, and J. P. Celis, *Wear*, **256**, 459 (2004).
15. A. Neville and X. Hu, *Wear*, **251**, 1284 (2001).
16. D. Landolt, S. Mischler, and M. Stemp, *Electrochim. Acta*, **46**, 3913 (2001).
17. N. Espallargas, R. Johnsen, C. Torres, and A. I. Muñoz, *Wear*, **307**, 190 (2013).
18. S. Mischler, *Tribol. Int.*, **41**, 573 (2008).
19. M. Salasi, G. Stachowiak, and G. Stachowiak, *Corros. Sci.*, **98**, 20 (2015).
20. G. Stachowiak, M. Salasi, and G. Stachowiak, in *5th World Tribology Congress, WTC 2013*, vol. **1** (2013).
21. M. Salasi, G. B. Stachowiak, and G. W. Stachowiak, in *18th International Corrosion Congress 2011*, vol. **2**, p. 1335 (2011).
22. A. R. Hind, S. K. Bhargava, and S. C. Grocott, *Colloids Surfaces A Physicochem. Eng. Asp.*, **146**, 359 (1999).
23. G. W. Stachowiak and A. W. Batchelor, *Engineering Tribology*, Elsevier, (2013).
24. I. M. Hutchings and P. Shipway, *Tribology: friction and wear of engineering materials*, p. 388 https://www-sciencedirect-com.dbgw.lis.curtin.edu.au/book/9780081009109/tribology.
25. M. Curioni, R. A. Cottis, M. Di Natale, and G. E. Thompson, *Electrochim. Acta*, **56**, 6318 (2011).
26. B. Cottis, *Corrosion*, **57**, 265 (2001).
27. C. O. A. Olsson and D. Landolt, *Electrochim. Acta*, **48**, 1093 (2003).
28. W. S. Tait, *An introduction to electrochemical corrosion testing for practicing engineers and scientists*, PairODocs Publications, (1994).
29. D. A. Jones, *Principles and Prevention of Corrosion*, 2nd ed., Prentice Hall, (1995).
30. J. Horvath and H. H. Uhlig, *J. Electrochem. Soc.*, **115**, 791 (1968).
31. R. Newman, in *Corrosion Chemistry Within Pits, Crevices and Cracks*, A. Turnbull, Editor, p. 317 (1984) http://scholar.google.com/scholar?hl=en&btnG=Search&q=intitle:Measurement+and+interpretation+of+electrochemical+kinetics+on+bare+metal+surfaces#0.
32. G. T. Burstein, C. Liu, R. M. Souto, and S. P. Vines, *Corros. Eng. Sci. Technol.*, **39**, 25 (2004).
33. G. S. Frankel, *J. Electrochem. Soc.*, **145**, 2186 (1998).
34. G. T. Burstein and S. P. Mattin, *Philos. Mag. Lett.*, **66**, 127 (1992).
35. G. S. Frankel, L. Stockert, and F. Hunkeler, **75**, 429 (2019).
36. M. Stemp, S. Mischler, and D. Landolt, *Wear*, **255**, 466 (2003).
37. V. M. Salinas-Bravo and R. C. Newman, *Corros. Sci.*, **36**, 67 (1994).
38. M. Iannuzzi, C. Mendez, L. Avila-Gray, G. Maio, and H. Rincón, *Corrosion*, **66**, 045003-045003–8 (2010).
39. M. Iannuzzi, J. Kovac, and G. S. Frankel, *Electrochim. Acta*, **52**, 4032 (2007).
40. P. Wu and J. P. Celis, *Wear*, **256**, 480 (2004).
41. F. Galliano, E. Galvanetto, S. Mischler, and D. Landolt, *Surf. Coatings Technol.*, **145**, 121 (2001).
42. S. S. Rajahram, T. J. Harvey, and R. J. K. Wood, *Tribol. Int.*, **44**, 232 (2011).
43. T. Adler and R. Walters, *Corros. Sci.*, **33**, 1855 (1992).
44. T. Adler and R. Walters, *Corrosion*, 49 (1993).
45. R. J. Chung, X. Tang, D. Y. Li, B. Hinckley, and K. Dolman, *Wear*, **271**, 1454 (2011).
46. E. Zumelzu et al., *Prot. Met.*, **39**, 183 (2003).
47. V. Marimuthu and K. Kannoorpatti, *J. Bio- Tribo-Corrosion*, **2**, 29 (2016).
48. G. Frankel, L. Stockert, F. Hunkeler, and H. Boehni, *Corrosion*, **18**, 429 (1987).